catalysts

MDPI

Article

Highly Porous SnO_2/TiO_2 Heterojunction Thin-Film Photocatalyst Using Gas-Flow Thermal Evaporation and Atomic Layer Deposition

Sungjin Kim [1,2], Hyeon-Kyung Chang [1,2], Kwang Bok Kim [3], Hyun-Jong Kim [1], Ho-Nyun Lee [1], Tae Joo Park [2] and Young Min Park [1,*]

[1] Heat and Surface Technology R&D Department, Korea Institute of Industrial Technology (KITECH), Incheon 21999, Korea; sungjin@kitech.re.kr (S.K.); hkjjj0902@gmail.com (H.-K.C.); hjkim23@kitech.re.kr (H.-J.K.); hnlee@kitech.re.kr (H.-N.L.)

[2] Department of Materials Science and Chemical Engineering, Hanyang University, Ansan 15588, Korea; tjp@hanyang.ac.kr

[3] Digital Health Care R&D Department, Korea Institute of Industrial Technology (KITECH), Cheonan 31056, Korea; kb815kim@kitech.re.kr

* Correspondence: youngmin@kitech.re.kr; Tel.: +82-10-4278-7958

Abstract: Highly porous heterojunction films of SnO_2/TiO_2 were prepared using gas-flow thermal evaporation followed by atomic layer deposition (ALD). Highly porous SnO_2 was fabricated by introducing an inert gas, Ar, during thermal evaporation. To build heterogeneous structures, the TiO_2 layers were conformally deposited on porous SnO_2 with a range of 10 to 100 cycles by means of ALD. The photocatalytic properties for different TiO_2 thicknesses on the porous SnO_2 were compared using the degradation of methylene blue (MB) under UV irradiation. The comparisons showed that the SnO_2/TiO_2-50 heterostructures had the highest photocatalytic efficiency. It removed 99% of the MB concentration, and the decomposition rate constant (K) was 0.013 min^{-1}, which was approximately ten times that of the porous SnO_2. On the other hand, SnO_2/TiO_2-100 exhibited a lower photocatalytic efficiency despite having a TiO_2 layer thicker than SnO_2/TiO_2-50. After 100 cycles of TiO_2 ALD deposition, the structure was transferred from the heterojunction to the core–sell structure covered with TiO_2 on the porous SnO_2, which was confirmed by TEM analysis. Since the electrons photogenerated by light irradiation were separated into SnO_2 and produced reactive oxygen, O_2^-, the heterojunction structure, in which SnO_2 was exposed to the surface, contributed to the high performance of the photocatalyst.

Keywords: photocatalyst; heterojunction; thermal evaporation deposition; atomic layer deposition; porous tin dioxide; titanium dioxide; core-shell structure

Citation: Kim, S.; Chang, H.-K.; Kim, K.B.; Kim, H.-J.; Lee, H.-N.; Park, T.J.; Park, Y.M. Highly Porous SnO_2/TiO_2 Heterojunction Thin-Film Photocatalyst Using Gas-Flow Thermal Evaporation and Atomic Layer Deposition. *Catalysts* **2021**, *11*, 1144. https://doi.org/10.3390/catal11101144

Academic Editors: Laura Bergamonti and Pier Paolo Lottici

Received: 30 August 2021
Accepted: 20 September 2021
Published: 23 September 2021

1. Introduction

Water contamination with dye discharges from various industries is considered a significant threat to the environment and public health [1,2]. Moreover, the scarcity of water resources has also become a major problem. Additionally, conventional wastewater treatment technologies have been problematic because of their long operation times and high costs [3,4]. Among the various dye-contaminated water treatment methods, photocatalytic degradation has attracted much attention for the removal of organic residues from wastewater. In particular, metal oxide heterojunctions employing advanced oxidation processes (AOPs) have been widely explored because of their rapid purification time and environmentally benign processes [5,6]. Under light irradiation, the heterojunction of a metal oxide semiconductor facilitates the separation of the generated electron–hole (e^-/h^+) pairs. These generated excitons produce reactive oxygen species in aqueous media, such as hydroxyl radicals (·OH) and superoxides ($\cdot O_2^-$), which are known to be photocatalytically active for the decomposition of organic contaminants, thereby purifying

dye-contaminated water [7–9]. Among various metal oxides, TiO_2 has been considered an attractive photocatalyst material for dye degradation because of its excellent catalytic activity and high chemical stability [10–15]. Under UV irradiation, the electrons generated by light absorption form a radical on the surface of TiO_2 near the energy level of the valence band, thus removing the dye from the water. However, the large band gap, ~3.2 eV, and fast recombination of the exciton of TiO_2 limit the photocatalytic efficiency. To resolve the low light adsorption and fast recombination of excitons in a single metal oxide, the heterostructures of TiO_2 with other metal oxide semiconductors, such as ZnO, and SnO_2, etc., have been explored using various synthesis methods. Metal oxide semiconductors with lower valence bands than TiO_2, such as SnO_2, facilitate the transfer of photogenerated holes in the valence band to TiO_2 in the heterojunction, thus hindering charge recombination and leading to efficient photocatalysis [16,17]. In addition to the selection of appropriate materials in heterojunctions, most research efforts in the field of photocatalysts have focused on optimizing microstructures to increase light absorption efficiency and to enlarge the active surface area using particle-type metal oxides. Since nanoparticle-type photocatalysts enlarge the active surface area and enhance light absorption, the synthesis of metal oxide nanoparticles has been widely investigated as a high-performance photocatalyst. However, despite their high performance, particle-type photocatalysts require additional separation processes in the suspension system, leading to high costs. Additionally, they cause secondary contamination resulting from the organic and inorganic binders in the synthesis and deposition process, thereby limiting their application [18–20]. Furthermore, most fabrication methods for particle-type heterojunctions involve complicated preparation processes and exhibit lower microstructure and chemical composition reproducibility [21]. Therefore, the development of a film-type photocatalyst with reproducibility is necessary to extend the usability and to improve the efficiency of the photocatalyst.

In this study, we fabricated a nanoporous SnO_2/TiO_2 heterojunction on a planar substrate using gas-flow thermal evaporation followed by atomic layer deposition (ALD) without binders. The flow of an inert gas, Ar, with a pressure of 0.2 Torr during thermal evaporation, allows the formation of a nanoporous structure. The conformal growth of TiO_2 on porous SnO_2 was demonstrated with a different cycle of ALD. In order to not cover the entire surface of SnO_2, TiO_2 was deposited with a lower number of ALD cycles, from 10 to 100 cycles, corresponding to a thickness of less than 2 nm. Chemical and microstructural analyses revealed the formation of the SnO_2/TiO_2 heterostructure. The evaluation of the photocatalytic activities of the as-prepared highly porous SnO_2/TiO_2 structures used the degradation of a methylene blue (MB) dye solution with a low UV irradiation intensity. Therefore, the results reveal that the heterostructure, not the core-shell structure of SnO_2/TiO_2, induces high photocatalytic activity, improves charge separation, and utilizes separated electrons and holes for photocatalysis in TiO_2 and SnO_2, respectively.

2. Results and Discussion

The highly porous heterojunction photocatalyst SnO_2/TiO_2 was fabricated by gas-flow-modified thermal evaporation followed by ALD. The plan-view and cross-sectional SEM images, Figure 1a,b, respectively, clearly show that the 3D nanoform microstructure of SnO_2 is well deposited with gas-flow-modified thermal evaporation at a pressure of 0.2 Torr. The surface area of the porous SnO_2 and SnO_2/TiO_2 was measured as about 74 m^2/g and 72.5 m^2/g with the Brunauer–Emmett–Teller method, respectively. The 50 cycles of ALD on the SnO_2 also did not significantly change the porosity of the SnO_2, as shown in Figure 1c,d, since the corresponding thickness by the ALD process is about 3 nm. On the other hand, the EDX elemental mapping on the SnO_2/TiO_2-50 clearly shows that the Ti atom was deeply distributed inside the matrix of the SnO_2 porous structure, indicating that the TiO_2 layer was conformally deposited on the porous nanostructure, as shown in Figure S1. In addition, transmission electron microscopy (TEM) analysis with electron energy loss spectroscopy showed that the TiO_2 layers were well deposited on the surface of the porous SnO_2 by ALD (Figure 2). As shown in Figure 2a, the nanoform of

SnO_2/TiO_2-100 shows that the TiO_2 layer is coated on the SnO_2 structure, with a thickness of approximately 1.3 nm. The growth rate of the TiO_2 on the porous SnO_2 structure is as low as one-third of that on the planar substrate because more precursors are required to cover the large surface area of the porous structure (Figure S2). Moreover, the electron energy loss spectroscopy spectrum showed that the TiO_2 was uniformly decorated on the whole surface of SnO_2, indicating that the TiO_2 deposition in 100 ALD cycles could fabricate a core-shell structure (Figure 2b–d. On the other hand, after ALD with less than 50 cycles, the particular structure of SnO_2 was not entirely covered by TiO_2 (Figure S3). The effect of microstructural changes with the number of ALD cycles on the photocatalytic performance will be further discussed in detail with the results of MB decomposition. The EDXRF analysis also showed that the Ti density increased with the number of ALD cycles, implying that the gradual growth of the TiO_2 layer with the number of ALD cycles was achieved on the porous structure (Figure 3). Note that the Ti density of sample after 100 cycles of ALD dramatically increases compared to other samples. Since the porous structure requires more cycles to move from the nucleation stage to the growth stage of ALD due to the larger surface area, it is expected that the SnO_2 nanoforms deposited through less than 50 cycles of ALD exhibit a different growth rate compared to SnO_2/TiO_2-100. The ALD as-synthesized TiO_2 layer was analyzed as the anatase phase using XRD, corresponding to JCPDS no. 21-1272 (Figure S4).

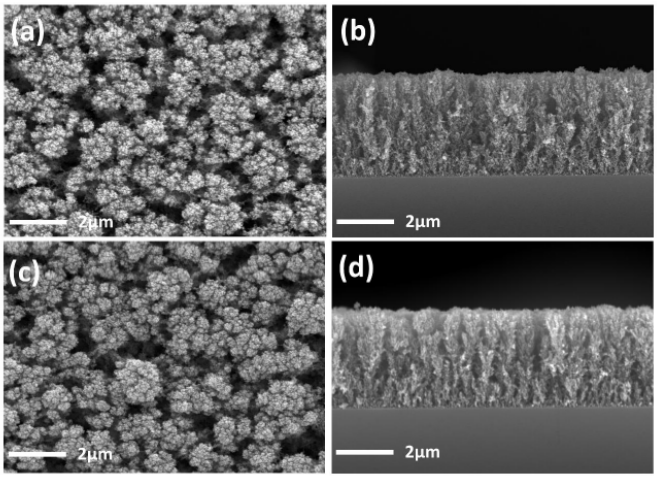

Figure 1. FE-SEM analysis of the porous SnO_2 and SnO_2/TiO_2-50. The surface section of (**a**) SnO_2 and (**c**) SnO_2/TiO_2-50 and the cross section of (**b**) SnO_2 and (**d**) SnO_2/TiO_2-50.

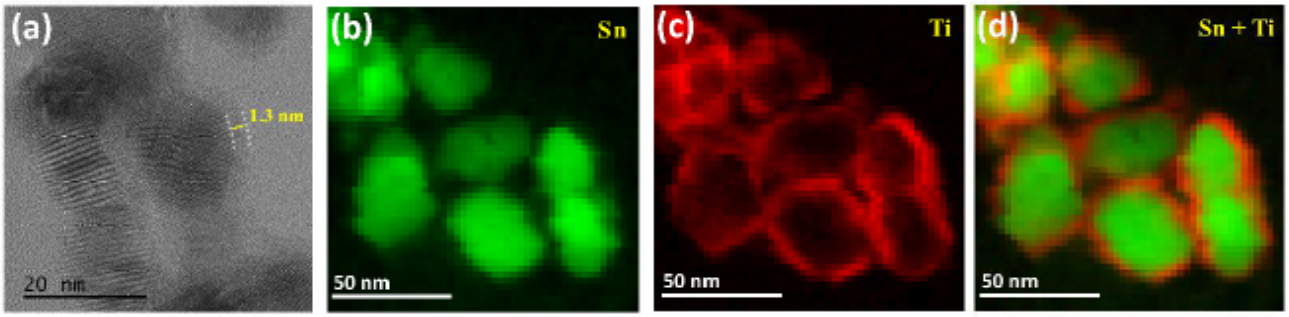

Figure 2. (**a**) The TEM image of SnO_2/TiO_2-100 and the EELS elemental mapping showing the elemental distribution of (**b**) Sn, (**c**) Ti, and (**d**) their overlay.

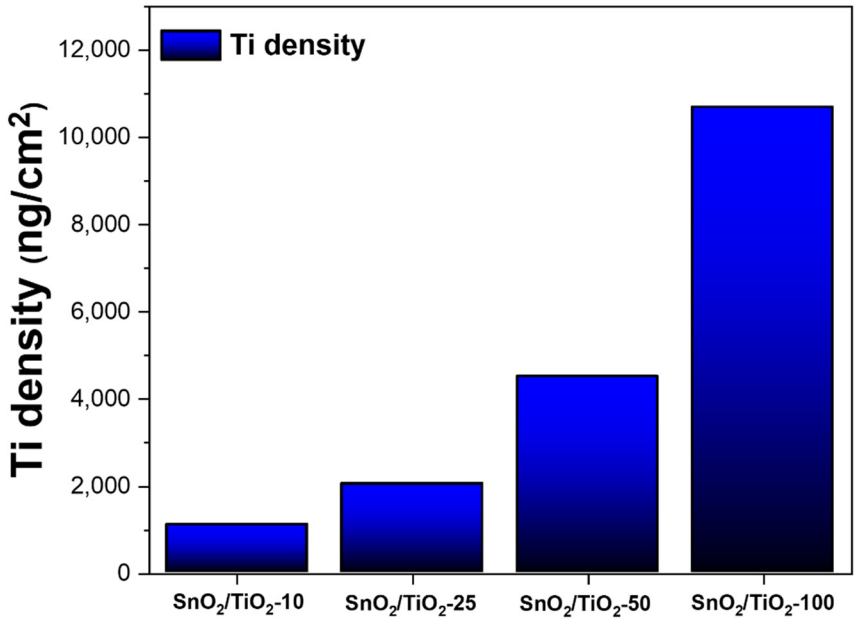

Figure 3. The Ti density of the SnO_2/TiO_2 photocatalysts analyzed using EDXRF. The Ti density increased with the number of TiO_2 ALD cycles.

The elemental chemical states of the constituent element, SnO_2/TiO_2, were determined using XPS for the different numbers of ALD cycles. As shown in Figure 4a, the two peaks of the Sn 3d spectra, 486.3 eV and 494.7 eV, assigned as Sn $3d_{5/2}$ and Sn $3d_{3/2}$, respectively, were observed in the spectra of the SnO_2/TiO_2-50 nanocomposite, implying that the porous SnO nanostructure was converted to the SnO_2 morphology after the annealing process. The two peaks of 458.4 eV and 464.1 eV corresponding to the peaks of Ti $2p_{3/2}$ and Ti $2p_{1/2}$ indicated successful TiO_2 deposition for the typical Ti^{4+}-O bond on the porous SnO_2 matrix, which is in good agreement with the EDXRF and EELS results (Figure 4b). As the amount of TiO_2 on the surface of the porous SnO_2 increased with the number of ALD cycles, a gradual shift of the Sn 3d peak toward a lower binding energy was observed, which was attributed to the donation of electrons to TiO_2 via the formation of Sn-O-Ti at the interface (Figure 4c,d) [22–24]. The introduction of TiO_2 on the surface of the SnO_2 induced an electron-rich environment at the interface, thereby lowering the binding energy of the SnO_2 3d electrons [25]. As shown in Figure 5, the XPS spectra for O 1s of pristine SnO_2 can be deconvoluted into two peaks with binding energies of 530.4 eV and 531.2 eV for the lattice oxygen (Lo) and oxygen vacancy or defect (Vo) of SnO_2, respectively [26]. The O 1s binding energy (530.4 eV) of SnO_2/TiO_2 gradually decreased with number of TiO_2 ALD cycles (Figure 5). Since TiO_2 has lower binding energy (529.8 eV) in the oxygen state than SnO_2, the formation of a TiO_2/SnO_2 heterojunction led to the formation of Sn-O-Ti bonding, thus exhibiting the lower binding energy of the Lo State. Hence, the Lo binding energy was substantially decreased in the SnO_2/TiO_2 heterostructure. The Vo state, implying an oxygen vacancy, on the other hand, slightly decreased with increasing TiO_2 layers, indicating that the deposition of TiO_2 reduced the oxygen vacancies and defects on the SnO_2 nanoform. Therefore, XPS analysis revealed that the ALD process not only induced the strongly bound heterojunction of SnO_2/TiO_2 but also reduced the surface defects of SnO_2, leading to efficient exciton separation and charge transfer.

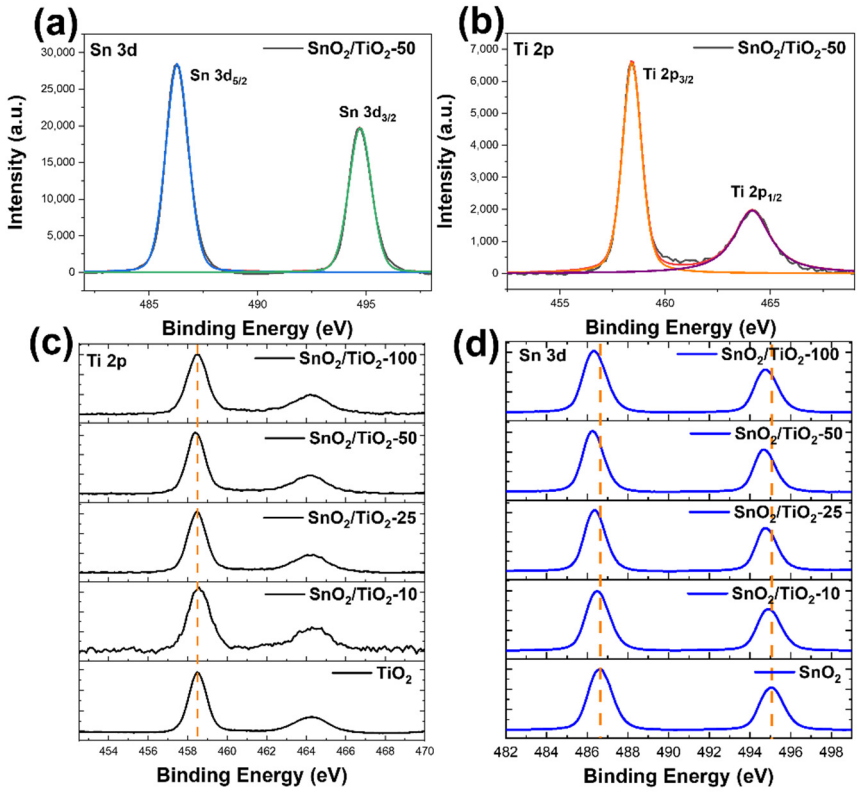

Figure 4. The XPS spectrum of the (**a**) Sn 3d and (**b**) Ti 2p states of the SnO_2/TiO_2-50 photocatalyst. The peak shift of (**c**) Ti 2p and (**d**) Sn 3d with the increase of TiO_2 ALD cycles.

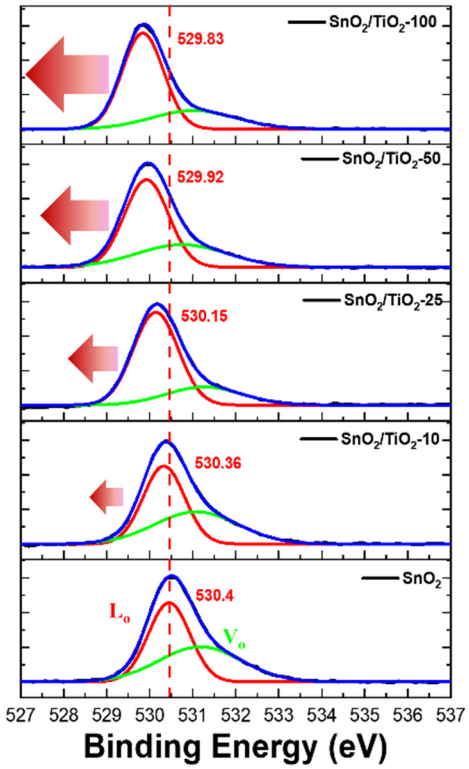

Figure 5. Comparison of the O 1s state of the SnO_2/TiO_2 photocatalysts with different TiO_2 ALD cycles from 10 to 100 cycles. The blue line was the chemical state of O 1s spectra and deconvoluted of lattice oxygen (Lo) and oxygen vacancy (Vo) which was indicated the red and green line, respectively.

The light absorption and band gap with different TiO_2 ALD cycles were measured using UV-vis absorption spectra, as shown in Figure 6. The SnO_2/TiO_2 samples showed strong absorption intensity at 320 nm with the increasing thickness of the TiO_2 nanoscale layers [27]. The nanoform of the porous SnO_2/TiO_2 induces more light absorption owing to the greater light pathway of the nanoporous structure. Additionally, the formation of a semiconducting heterojunction structure with TiO_2 enhances the absorption intensity at approximately 400 nm. For better understanding, the optical band gaps of the SnO_2/TiO_2 samples were experimentally determined using the linear portion of the Kubelka–Munk function. The measured optical band gap of the porous SnO_2 nanoform was 3.2 eV whereas all the SnO_2/TiO_2 photocatalysts had lower band gaps. Further, the SnO_2/TiO_2-10, 25, 50, and 100 samples were slightly shifted toward shorter band gap, with the increasing TiO_2 layer at 3.03, 2.93, 2.88, and 3.00 eV, respectively. However, the SnO_2/TiO_2-100 samples displayed a wavelength shift toward a larger band gap, which indicated that the thick layer of TiO_2 caused less light scattering in the pores and decreased light reflection pathways [28,29].

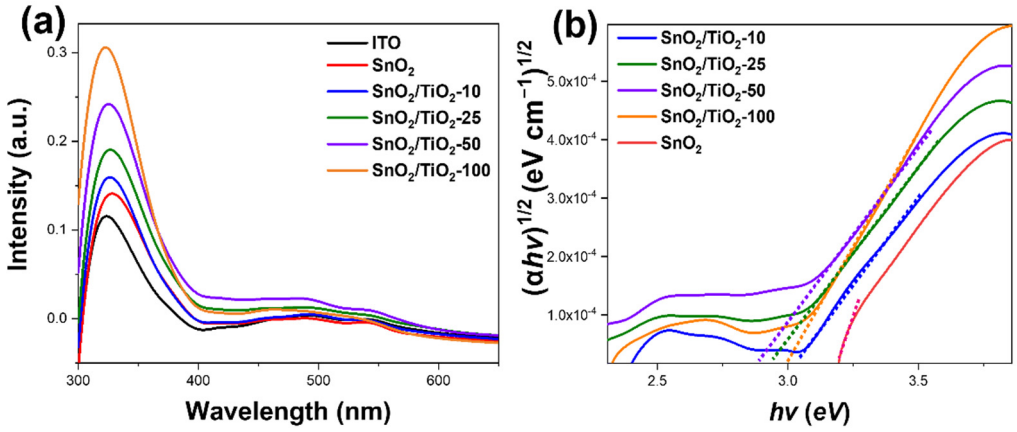

Figure 6. (**a**) UV-vis absorption spectra of the porous SnO_2 and all the SnO_2/TiO_2 photocatalysts on the ITO substrate. (**b**) Calculation of the optical bandgap from the UV-vis absorption spectra of the porous SnO_2 nanofoam and all of the the SnO_2/TiO_2 photocatalysts.

The photocatalytic performance of the highly porous SnO_2/TiO_2-10, 25, 50, and 100 heterojunction films was evaluated using the degradation of the MB solution under UV light irradiation (Figure 7). While the MB solution was barely degraded without the catalysts, the porous SnO_2 nanofoam exhibited a 60% MB degradation after 300 min, and the presence of all of the porous SnO_2/TiO_2 nanofoams enhanced photocatalytic activity compared to the bare SnO_2 nanofoam due to the synergistic effect between the SnO_2 and TiO_2 heterojunction. The time-dependent UV-vis absorbance spectra of MB degradation displayed a significant reduction in the MB concentration, as shown in Figure S5. The photocatalytic efficiency (η)% of the photocatalyst was calculated from $\eta = (C_0 - C)/C \times 100$, where C_0 is the initial concentration of MB, and C is the remaining concentration of MB after photocatalysis. As confirmed in Figure 6 and Figure S6, the SnO_2/TiO_2-50 heterostructure photocatalyst displays the highest photocatalytic efficiency (99%) compared to SnO_2/TiO_2-10 (73%), SnO_2/TiO_2-25 (91%), SnO_2/TiO_2-100 (81%), and SnO_2 (60%) after photocatalysis. Comparing the photocatalytic reaction rate, which follows pseudo first order reaction kinetics and is expressed as $\ln(C_0/C) = -Kt$, where K is apparent rate constant, and t is the time interval, the decomposition rate constant K values were 0.0030, 0.0042, 0.0078, 0.013, and 0.0056 min^{-1} for the SnO_2, SnO_2/TiO_2-10, 25, 50, and 100 photocatalysts, respectively (Table 1). The rate constant of SnO_2/TiO_2-50 was approximately two times higher than that of the core-shell SnO_2/TiO_2-100 and had the highest reaction rate compared to the as-fabricated photocatalysts. It is generally acknowledged that photoexcited electrons and holes play a key role in photocatalytic reduction reactions, as they generate lots of

main reactive species that are involved in photocatalytic oxidation, such as $\cdot O_2^-$ and ·OH. The low photocatalytic efficiency of the porous SnO_2 films is attributed to conduction band of the SnO_2, which has lower electric potential compared to the O_2/O_2^- oxidation potential, although the holes in valence band of SnO_2 oxidized the organic pollutant directly using the ·OH radical to contribute to the performance [30]. On the contrary, the SnO_2/TiO_2 heterojunction gives rise to charge separation due to the potential difference, hence increasing the lifetime of the charge carrier and improving the interfacial charge transfer to the adsorbed surface. The photogenerated electrons and holes of the SnO_2/TiO_2 heterojunction produced strong oxidizing radicals of $\cdot O_2^-$ and ·OH from the water or oxygen on the surface of SnO_2 and TiO_2, respectively, thereby degrading the organic pollutant (Figure 8) [31,32]. Since the ·OH radical generated in the valence band of TiO_2 is a stronger oxidant, the introduction of the TiO_2 layer can improve the photocatalytic efficiency. In addition, light absorption was enhanced by increasing the thickness of the TiO_2. Therefore, more ALD cycles of TiO_2 induce more active sites for TiO_2 and light absorption, thereby improving the photocatalytic performance, as shown in Figure 6. Note that the SnO_2/TiO_2-100 photocatalyst had a lower MB degradation performance than the SnO_2/TiO_2-50 despite the thicker TiO_2 layers and greater light absorption. As shown in Figure 2, 100 cycles of the ALD process produced a core-shell structure and removed the surface of SnO_2, which was used to generate $\cdot O_2^-$ oxidizing radicals from the transfer of photogenerated electrons. Furthermore, the thicker TiO_2 layer of SnO_2/TiO_2-100 hinders the charge transfer to the surface of the TiO_2 layer to degrade MB. Therefore, the SnO_2/TiO_2-50 heterojunction structure possessing both the TiO_2 and SnO_2 surfaces is advantageous for efficient photocatalysis since it has enhanced light absorption and more oxidizing radicals from both the photogenerated electrons and holes.

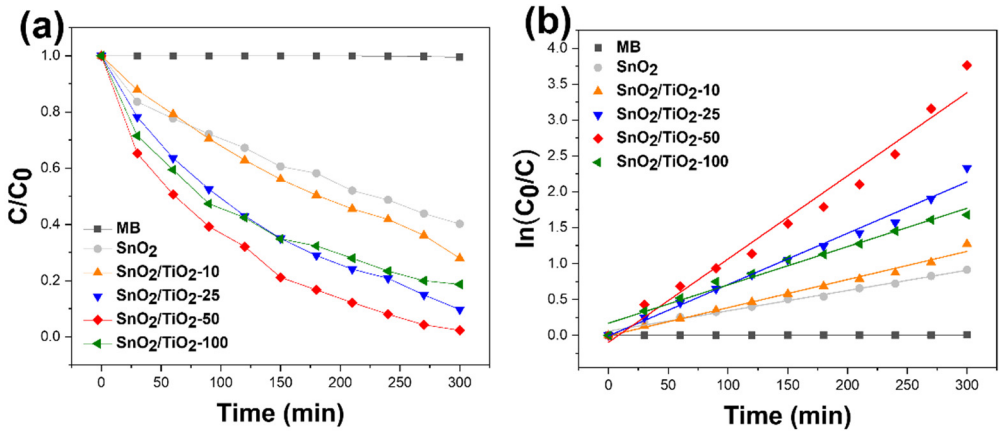

Figure 7. (**a**) Decomposition of the MB concentration ratio (C/C_0) and (**b**) the kinetics of the photocatalytic degradation of MB by all the SnO_2/TiO_2 photocatalysts with different TiO_2 ALD cycles.

Table 1. Comparison of the photocatalytic efficiency (%) and decomposition reaction rate (*K*) of the porous SnO_2 nanofoam and SnO_2/TiO_2-10, 25, 50, and 100 heterojunction films.

	MB	SnO_2	SnO_2/TiO_2-10cyc	SnO_2/TiO_2-25cyc	SnO_2/TiO_2-50cyc	SnO_2/TiO_2-100cyc
Photo-catalytic efficiency (%)	<1	60	73	91	99	81
K (min^{-1})	N/A	0.0030	0.0042	0.0078	0.013	0.0056

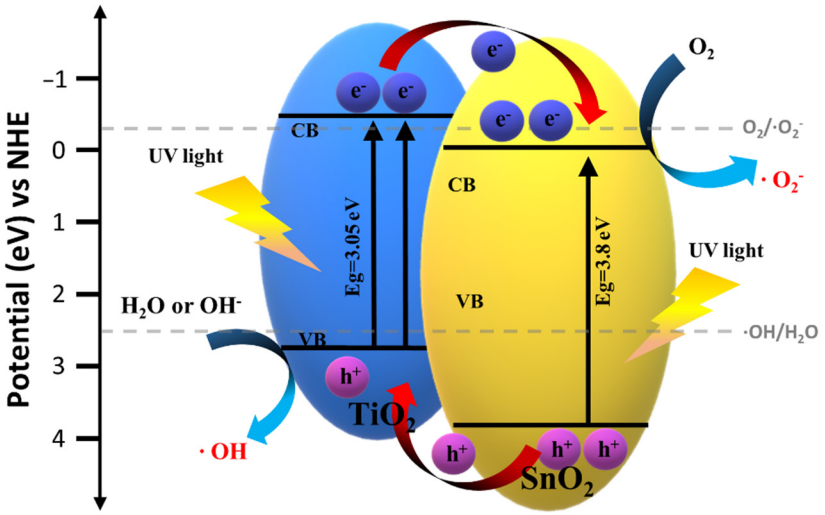

Figure 8. Band diagram of the SnO_2/TiO_2 heterojunction and photocatalysis mechanism.

3. Experimental Section

3.1. Chemical and Substrate

Pure tin oxide (SnO) (0.2 g, 99.995% pure, LTS Research Laboratories, Inc., USA) was used as the thermal evaporation material. The titanium tetra-isopropoxide (TTIP) precursor for ALD was purchased from UP Chemical Co., Ltd., Pyeongtaek, Korea. The porous SnO films were fabricated on Si (100) wafers or ITO substrates with the dimensions of 2×2 cm^2. The substrate was cleaned thoroughly with deionized water, acetone, and ethanol for 10 min and were dried by blowing N_2 over the sample. The UV-vis absorption spectra were measured using a SnO_2/TiO_2 photocatalyst on an indium-doped tin oxide (ITO) substrate (7–10 ohm/sq, transmittance: 80–85%).

3.2. Preparation of Porous SnO_2 Nanoform

The highly porous SnO nanoform was fabricated by Ar-assisted modified thermal evaporation, as previously reported [33,34]. The SnO source was kept in a Ta boat, which was subsequently placed at the center of the chamber, and the Si/SiO_2 substrate was placed at the upper site, with the cooling system at 23 °C. During thermal evaporation, the highly pure Ar gas (99.9999%) flowed with 100 sccm to reach a pressure of 0.2 Torr after evacuation to a 5×10^{-6} Torr pressure, and the SnO source was rotated at a speed of 8 rpm in order to form a uniform nanoporous structure. After thermal deposition, the porous SnO nanoform was annealed at 700 °C for 1 h with 50 sccm pure air in a tube furnace to obtain the SnO_2 crystallite structure.

3.3. Preparation of the Porous SnO_2/TiO_2 Heterostructure

The highly porous SnO_2/TiO_2-10, 25, 50 and 100 heterostructure films was synthesized by atomic layer deposition with a different number of cycles on the porous SnO_2 nanofoam. The TTIP and deionized water were used as the metal precursor and oxygen source, respectively. Highly pure N_2 gas (99.9999%) was used for the purge process with a gas flow rate of 200 sccm. The as-synthesized porous SnO_2 film was kept at 300 °C in a reaction chamber, and the base pressure was maintained at 1.5×10^{-2} torr using a dry pump (Edwards, IQDP80, Edwards. Co., United Kingdom). In order to control the uniformity and thickness of the TiO_2 layer, it was coated with a highly porous SnO_2 nanocomposite with 10, 25, 50, and 100 cycles of ALD, denoted as SnO_2/TiO_2-10, SnO_2/TiO_2-25, SnO_2/TiO_2-50, and SnO_2/TiO_2-100, respectively.

3.4. Evaluation of Photocatalytic Activity

The photocatalytic properties of the as-synthesized SnO_2/TiO_2-10, 25, 50, and 100 films were evaluated by the degradation of MB under UV light irradiation (265 nm) in a cooling bath. MB (1.2 mg) was dissolved in 1 L of deionized water and was stirred for 2 h in the dark. Before evaluating the photocatalytic properties, the porous SnO_2/TiO_2 heterostructured films were kept in 50 mL of MB solution and were stirred for 30 min in the dark to achieve adsorption–desorption equilibrium. After UV irradiation with a power of 16 W, the solution was characterized by UV-vis absorbance spectroscopy (UV-2500 UV-vis spectrophotometer, Shimadzu. Co., Japan) to evaluate the photodegradation of MB.

3.5. Materials Characterization

The microstructure of the SnO_2/TiO_2 nanoform was characterized by field-emission scanning electron microscopy (FE-SEM, JEOL JSM-7100F, JEOL Co., Japan) with energy dispersive X-ray spectroscopy (EDS) mapping. Elemental mapping analysis of SnO_2/TiO_2 from electron energy loss spectroscopy (EELS) were conducted using a ZEISS Libra 200 HT Mc Cs, Zeiss, Co., Germany (200 kV)/JEOL ARM 200 F, JEOL. Co., Japan (200 kV). The chemical binding energy of the SnO_2/TiO_2 nanoform with the number of TiO_2 deposition cycles was analyzed through X-ray photoelectron spectroscopy (XPS) using a K-alpha plus (ESCALAB 250Xi, Thermo Fisher Scientific. Co., USA) instrument utilizing monochromatic Al Kα (1486.6 eV) radiation. The surface composition of Ti in SnO_2/TiO_2 was determined using a Rigaku ZSX Primus II energy-dispersive X-ray fluorescence (EDXRF) spectrometer (Rigaku. Co., Japan).

4. Conclusions

A highly porous SnO_2/TiO_2 heterojunction structure was synthesized using gas flow thermal evaporation and ALD, which controlled the TiO_2 thickness on the porous SnO_2 structure. Owing to the charge separation that leads to the formation of radicals, the heterojunction structure with a TiO_2 layer on SnO_2 exhibited a higher photocatalytic efficiency than bare SnO_2. The effect of TiO_2 thickness on the photocatalytic activity was also investigated. According to the results, SnO_2/TiO_2-50, which was analyzed to have TiO_2 deposited sparsely on the porous SnO_2, had the highest kinetic constant of 0.013 min^{-1}, which was two times higher than that of the core-shell structure of SnO_2/TiO_2-100. The facile separation of the electron/hole pairs and corresponding oxygen radicals on the surface of both TiO_2 and SnO_2 can improve the photocatalytic activity in the heterojunction compared to the core-shell structure.

Supplementary Materials: The following are available online at https://www.mdpi.com/article/10.3390/catal11101144/s1, Figure S1: EDX mapping for SnO_2/TiO_2-50: (a) lateral SEM image of SnO_2/TiO_2-50 of information collection area, (b) O element, (c) Si element (d) Sn element, and (e) Ti element, Figure S2: Growth per cycle (GPC) of TiO_2 thin film at 300 °C on Si substrate, Figure S3: EELS spectrum of SnO_2/TiO_2-50. Sn and Ti clearly reveal presence as heterojunction structure, Figure S4: XRD pattern of as-deposited TiO_2 layer by ALD cycles process on Si substrate, Figure S5: UV-Visible absorbance spectra of photodegradation of methylene blue (a–e) by SnO_2 and all SnO_2/TiO_2 with different ALD cycles, Figure S6: The photocatalytic efficiency (%) with increasing degradation time by SnO_2 and all SnO_2/TiO_2-50 photocatalysts.

Author Contributions: Conceptualization, S.K. and Y.M.P.; methodology, S.K., H.-K.C. and H.-J.K.; validation, S.K., K.B.K. and H.-N.L.; formal analysis, S.K.; investigation, S.K., K.B.K., T.J.P. and Y.M.P.; data curation, S.K.; writing—original draft preparation, S.K. and Y.M.P.; writing—review and editing, S.K. and Y.M.P.; project administration, Y.M.P.; All authors have read and agreed to the published version of the manuscript.

Funding: This research was financially supported by the Basic Research Program of the Korea National Research Foundation (Project No. NRF-2020R1F1A1067830).

Conflicts of Interest: The authors declare no conflict of interest.

References

1. Rasheed, T.; Bilal, M.; Nabeel, F.; Adeel, M.; Iqbal, H.M.N. Environmentally-related contaminants of high concern: Potential sources and analytical modalities for detection, quantification, and treatment. *Environ. Int.* **2019**, *122*, 52–66. [CrossRef]
2. Khan, S.; Malik, A. Toxicity evaluation of textile effluents and role of native soil bacterium in biodegradation of a textile dye. *Sci. Pollut. Res.* **2018**, *25*, 4446–4458. [CrossRef] [PubMed]
3. Hodeges, B.C.; Cates, E.L.; Kim, J.-H. Challenges and prospects of advanced oxidation water treatment processes using catalytic nanomaterials. *Nat. Nanotechnol.* **2018**, *13*, 642–650. [CrossRef] [PubMed]
4. Mashuri, S.I.S.; Ibrahim, M.L.; Kasim, M.F.; Mastuli, M.S.; Rashid, U.; Abrullah, A.H.; Islam, A.; Mijan, N.A.; Tan, Y.H.; Mansir, N.; et al. Photocatalysis for organic wastewater treatment: From the basis to current challenges for society. *Catalysts* **2020**, *10*, 1260. [CrossRef]
5. Chan, S.H.S.; Wu, T.Y.; Juna, J.C.; Teh, C.Y. Recent developments of metal oxide semiconductors as photocatalysts in advanced oxidation processes (AOPs) for treatment of dye waste-water. *J. Chem. Technol. Biotechnol.* **2011**, *86*, 1130–1158. [CrossRef]
6. Martini, J.; Orge, C.A.; Faria, J.L.; Rereira, M.F.R.; Soares, O.S.G.P. Catalytic advanced oxidation processes for sulfamethoxazole degradation. *Appl. Sci.* **2019**, *9*, 2652. [CrossRef]
7. Loeb, S.K.; Alvarez, P.J.J.; Brame, J.A.; Cates, E.L.; Choi, W.; Crittenden, J.; Dionysiou, D.D.; Li, Q.; Puma, G.L.; Quan, X.; et al. The Technology horizon for photocatalytic water treatment: Sunrise or sunset? *Environ. Sci. Technol.* **2019**, *53*, 2937–2947. [CrossRef]
8. Wang, Y.; Wang, Q.; Zhan, W.; Wang, F.; Safdar, M.; He, J. Visible light driven type II heterostructures and their enhanced photocatalysis properties: A review. *Nanoscale* **2013**, *5*, 8326–8339. [CrossRef]
9. Nosaka, Y.; Nosaka, A. Understanding hydroxyl radical (·OH) generation processes in photocatalysis. *ACS Energy Lett.* **2016**, *1*, 356–359. [CrossRef]
10. Ong, C.B.; Ng, L.Y.; Mohammad, A.W. A review of ZnO nanoparticles as solar photocatalysts: Synthesis, mechanisms and applications. *Renew. Sustain. Energy. Rev.* **2018**, *81*, 536–551. [CrossRef]
11. Tian, C.; Zhang, Q.; Wu, A.; Jiang, M.; Liang, Z.; Jiang, B.; Fu, H. Cost-effective large-scale synthesis of ZnO photocatalyst with excellent performance for dye photodegradation. *Chem. Commu.* **2012**, *48*, 2858–2860. [CrossRef]
12. Vaseem, M.; Umar, A.; Hahn, Y.B.; Kim, D.H.; Lee, K.S.; Jang, J.S.; Lee, J.S. Flower-shaped CuO nanostructures: Structural, photocatalytic and XANES studies. *Catal. Commun.* **2008**, *10*, 11–16. [CrossRef]
13. Ramesh, M.; Rao, M.P.C.; Anandan, S.; Nagaraja, H. Adsorption and photocatalytic properties of NiO nanoparticles synthesized via a thermal decomposition process. *J. Mater. Res.* **2018**, *33*, 601–610. [CrossRef]
14. Liu, Y.; Wang, M.; Li, D.; Fang, F.; Huang, W. Engineering self-doped surface defects of anatase TiO_2 nanosheets for enhanced photocatalytic efficiency. *Appl. Surf. Sci.* **2021**, *540*, 148330. [CrossRef]
15. Schneider, J.; Matsuoka, M.; Takeuchi, M.; Zhang, J.; Horiuchi, Y.; Anpo, M.; Bahnemann, D.W. Understanding TiO_2 photocatalysis: Mechanisms and materials. *Chem. Rev.* **2014**, *114*, 9919–9986. [CrossRef]
16. Shi, H.; Zhou, M.; Song, D.; Pan, X.; Fu, J.; Zhou, J.; Ma, S.; Wang, T. Highly porous SnO_2/TiO_2 electrospun nanofibers with high photocatalytic activities. *Ceram. Int.* **2014**, *40*, 10383–10393. [CrossRef]
17. Cheng, H.-E.; Lin, C.-Y.; Hsu, C.-M. Fabrication of SnO_2-TiO_2 core-shell nanopillar array films for enhanced photocatalytic activity. *Appl. Sur. Sci.* **2017**, *396*, 393–399. [CrossRef]
18. Malagutti, A.R.; Mourão, H.A.J.L.; Garbin, J.R.; Ribeiro, C. Deposition of TiO_2 and Ag:TiO_2 thin films by the polymeric precursor method and their application in the photodegradation of textile dyes. *Appl. Catal. B* **2009**, *90*, 205–212. [CrossRef]
19. Dey, N.K.; Kim, M.J.; Kim, K.-D.; Seo, H.O.; Kim, D.H.; Kim, Y.D.; Lim, D.C.; Lee, K.H. Adsorption and photocatalytic degradation of methylene blue over TiO_2 films on carbon fiber prepared by atomic layer deposition. *J. Mol. Catal. A Chem.* **2011**, *337*, 33–38. [CrossRef]
20. Arekhi, M.; Jamshidi, M. Influences of inorganic binder on photocatalytic oxidation (PCO) and degradation of nano/micro TiO_2 containing acrylic composites. *Prog. Org. Coat.* **2018**, *115*, 1–8. [CrossRef]
21. Zhao, W.; Liu, Y.; Wei, Z.; Yang, S.; He, H.; Sun, C. Fabrication of a novel p-n heterojunction photocatalyst n-$BiVo_4$@p-MoS_2 with core-shell structure and its excellent visible-light photocatalytic reduction and oxidation activities. *Appl. Catal. B* **2016**, *185*, 242–252. [CrossRef]
22. Wang, H.-B.; Ma, F.; Sun, Y.-S.; Zhou, L.; Zeng, D.-J.; Qin, Y.; Xu, Y.-K.; Chen, Y.-N.; Xu, K.-W.; Ma, D.-Y. Band bending and valence band shifting of sub-monolayer TiO_2 functionalized SnO_2 nanowires. *J. Mater. Sci. Mater. Electron.* **2020**, *31*, 637–643. [CrossRef]
23. Yu, Y.; Ma, K.; RZhuang, R.; Wu, K.; Liao, Q.; Zhong, S.; Yue, H.; Liu, C.; Tang, S.; Liang, B. Hydroxyl-mediated formation of highly dispersed SnO_2/TiO_2 heterojunction via pulsed chemical vapor deposition to enhance photocatalytic activity. *Ind. Eng. Chem. Res.* **2019**, *58*, 14655–14663. [CrossRef]
24. Du, H.; Yao, P.; Sun, Y.; Wang, J.; Wang, H.; Yu, N. Electrospinning hetero-nanofibers In_2O_3/SnO_2 of homotype heterojunction with high gas sensing activity. *Sensors* **2017**, *17*, 1822. [CrossRef] [PubMed]
25. Zhang, Z.; Ma, Y.; Bu, X.; Wu, Q.; Hang, Z.; Dong, Z.; Wu, X. Facile one-step synthesis of $TiO_2/Ag/SnO_2$ ternary heterostructures with enhanced visible light photocatalytic activity. *Sci. Rep.* **2018**, *8*, 10532. [CrossRef] [PubMed]
26. Ghobadi, A.; Ulusoy, T.G.; Garifullin, R.; Guler, M.O.; Okyay, A.K. A heterojunction design of single layer hole tunneling ZnO passivation wrapping around TiO_2 nanowires for superior photocatalytic performance. *Sci. Rep.* **2016**, *6*, 30587. [CrossRef]

27. Chen, Y.; Wang, Y.; Li, W.; Yang, Q.; Hou, Q.; Wei, L.; Liu, L.; Huang, F.; Ju, M. Enhancement of photocatalytic performance with the use of noble-metal-decorated TiO_2 nanocrystals as highly active catalysts for aerobic oxidation under visible. *Appl. Catal. B* **2017**, *210*, 352–367. [CrossRef]
28. Wang, X.; Ni, Q.; Zeng, D.; Liao, G.; Wen, Y.; Shan, B.; Xie, C. BiOCl/TiO_2 heterojunction network with high energy facet exposed for highly efficient photocatalytic degradation of benzene. *Appl. Surf. Sci.* **2017**, *296*, 590–598. [CrossRef]
29. Wang, J.; Zhao, J.; Li, Y.; Yang, M.; Chang, Y.-Q.; Zhang, J.-P.; Sun, Z.; Wang, Y. Enhanced light absorption in porous particles for Ultra-NIR-Sensitive biomaterials. *ACS Macro. Lett.* **2015**, *4*, 392–397. [CrossRef]
30. Kim, S.P.; Choi, M.Y.; Choi, H.C. Photocatalytic activity of SnO2 nanoaprticles in methylene blue degradation. *Mater. Res. Bull.* **2016**, *74*, 85–89. [CrossRef]
31. Lv, L.; Bai, X.; Ye, Z. Construction of N-doped TiO_2/SnO_2 heterostructured microspheres with dominant {001} facets for enhanced photocatalytic properties. *CrystEngComm* **2016**, *39*, 7580–7589. [CrossRef]
32. Alagarasi, A.; Rajalakshmi, P.U.; Shanthi, K.; Selvam, P. Solar-light driven photocatalytic activity of mesoporous nanocrystalline TiO_2, SnO_2, and TiO_2-SnO_2 composites. *Mater. Today Sustain.* **2019**, *5*, 100016. [CrossRef]
33. Park, Y.M.; Hwang, S.H.; Lim, H.; Lee, H.-N.; Kim, H.-J. Scalable and Versatile Fabrication of Metallic Nanofoam Films with Controllable Nanostructure Using Ar-Assisted Thermal Evaporation. *Chem. Mater.* **2020**, *33*, 205–211. [CrossRef]
34. Chang, H.-K.; Ko, D.-S.; Cho, D.-H.; Kim, S.; Lee, H.-N.; Lee, H.S.; Kim, H.-J.; Park, T.J.; Park, Y.M. Enhanced response of the photoactive gas sensor on formaldehyde using porous SnO_2@TiO_2 heterostructure driven by gas-flow thermal evaporation and atomic layer deposition. *Ceram. Int.* **2021**, *47*, 5958–5992. [CrossRef]